Performances of motion tracking enhanced Tomo-PIV on turbulent shear flows

Matteo Novara · Fulvio Scarano

Abstract The motion tracking enhancement technique (MTE) is a recently introduced method to improve the accuracy of tomographic PIV measurements at seeding density higher than currently practiced. The working principle is based on the fact that the particle field and its projections are correlated between the two exposures. Therefore, information from subsequent exposures can be shared within the tomographic reconstruction process of a single object, which largely reduces the energy lost into *ghost particles*. The study follows a previous work based on synthetic particle images, showing that the MTE technique has an effect similar to that of increasing the number of cameras. In the present analysis, MTE is applied to Tomographic PIV data from two time-resolved experiments on turbulent shear flows: a round jet at $Re = 5{,}000$ ($f_{acq} = 1{,}000$ Hz) and a turbulent boundary layer at the trailing edge of an airfoil ($Re_c = 370{,}000$) measured at 12,000 Hz. The application of MTE is extended to the case of more than two recordings. The performance is assessed comparing the results from a lowered number of cameras with respect to the full tomographic imaging system. The analysis of the jet flow agrees with the findings of numerical simulations provided the results are *scaled* taking into account the concept of MTE efficiency based on the volume fraction where *ghost-pairs* (Elsinga et al. 2010a) are produced. When a large fraction of fluid has uniform motion (stagnant fluid surrounding the jet), only a moderate reduction in *ghost intensity* is expected by MTE. Nevertheless, a visible recovery of reconstruction quality is observed for the 3-cameras system when MTE is applied making use of 3 recordings. In the turbulent boundary layer, the objective is set to increase the seeding density beyond current practice, and the experiments are performed at approximately 200,000 particles/megapixel. The measurement robustness is monitored with the signal-to-noise ratio S/N for the cross-correlation analysis. An estimate of the precision error is obtained for the turbulent boundary layer case following the peak height of the spatio-temporal cross-correlation function (*frozen-turbulence*). The MTE approach appears to be essential for the increase in robustness and measurement precision at such seeding density.

1 Introduction

Tomographic PIV (Tomo-PIV) is an established three-dimensional variant of PIV enabling instantaneous access to the three velocity component in a volumetric domain (Elsinga et al. 2006). Illuminated particles are simultaneously viewed from several directions. The 3D intensity distribution of particles (object) is most commonly reconstructed using the MART algorithm (Herman and Lent 1976) although recent works have investigated faster reconstruction methods (Worth and Nickels 2008; Atkinson and Soria 2009) or algorithms that may further improve the reconstruction accuracy (Petra et al. 2009). The particles motion analysis is typically performed by 3D cross-correlation of the pair of reconstructed objects. In comparison with other 3D-PIV approaches, such as Digital Holographic PIV (Coëtmellec et al. 2001) and 3D particle tracking (Maas et al. 1993), or Defocusing Digital PIV (DDPIV, Pereira and Gharib 2002) Tomo-PIV allows measurements with a higher concentration of seeding

M. Novara (✉) · F. Scarano
Department of Aerospace Engineering,
Delft University of Technology,
Delft, The Netherlands
e-mail: M.Novara@tudelft.nl

tracers (typically 50,000 particles/megapixel), providing the spatial resolution required to characterize the coherent motion of turbulent flows (Scarano et al. 2006; Elsinga et al. 2008; Schröder et al. 2008; Scarano and Poelma 2009) also at very high Reynolds number (Humble et al. 2009; Elsinga et al. 2010a, b). The robustness of Tomo-PIV strongly relies upon a high-precision camera calibration, which is obtained with a digital correction procedure to the sliding target calibration (Volume Self-Calibration, Wieneke 2008). When compared with planar PIV, the reliability and accuracy of Tomographic PIV strongly depends upon the density of imaged particles on the source (source density N_S, Adrian 1991). Experiments performed in the past years showed that a seeding density such that approximately 30% of the sensor is occupied by particle images ($N_S \sim 0.3$) can be accurately reconstructed and their motion faithfully tracked by spatial cross-correlation. It is also well known that an excessive particle image density ($N_S \sim 1$) compromises the reconstruction and returns a low quality factor Q (Elsinga et al. 2006), which results in largely inaccurate velocity vector field. As a consequence, the current best practice suggests that the image seeding density should typically not exceed 50,000 particles/megapixel ($ppp < 0.05$).

For a higher seeding density, the main source of error in the tomographic reconstruction process is represented by the formation of ghost particles (Elsinga et al. 2008), a phenomenon already investigated in 3D-PTV studies (Maas et al. 1993, among others): spurious intensity is reconstructed at the intersection of lines-of-sight crossing actual particles. Such ghost particles also degrade the intensity field of the actual particles in that the projection of the overall intensity must match the intensity on the images. A consequence of the ghost particles is that they may affect the cross-correlation signal, introducing random and bias errors in the velocity field, as demonstrated in the recent study from Elsinga et al. (2010a, b). The number of ghost particles in a reconstructed intensity field depends upon several experimental parameters, mostly the number of simultaneous views N_C and the seeding particles concentration (Elsinga et al. 2006). Therefore, the phenomenon of ghost particles formation currently represents one of the largest obstacles to increasing the spatial resolution of Tomo-PIV measurements and as such it has received considerable attention. Increasing the number of simultaneous views of the tomographic system may be regarded as a possible solution, provided that the system complexity and costs remain affordable.

The main difference between regular tomography and Tomo-PIV is that the latter is always based upon two or more subsequent recordings of the object (particles field). Although the particles position changes in between the exposures, one may reasonably assume that the same set of particles is illuminated at the two time instants. This leads to the concept of *fluid object*, that is exploited by the recently proposed, Motion Tracking Enhancement, (*MTE*, Novara et al. 2010), which combines two or more non-simultaneous recordings of the particles for the reconstruction of each instantaneous particle field. The MTE technique was reported to increase in robustness and accuracy of MART-based Tomo-PIV at higher seeding density than possible with the MART algorithm only. In the above work, the working principle of the MTE method and its potential were scrutinized by simulations based on synthetic images, which showed considerable improvements in terms of reconstruction quality. The results also reported a significant reduction in the precision error in the velocity field. Real imaging effects and calibration errors were not taken into account in the numerical simulations. Moreover, in Tomo-PIV experiments, the flow field characteristics are unknown, and the seeding density can be underestimated; therefore, the extrapolation of results from simulations to real experiments remained to be ascertained. A preliminary analysis of the MTE performances applied on data from a jet flow in water at Reynolds 5,000 was also included, showing the potential of the technique in increasing the quality of the reconstruction and reducing the measurement uncertainty.

In the present study, the Motion Tracking Enhancement is applied extensively to two experiments conducted in water and in air flows. The first experiment is a transitional jet in a water flow and the second is a turbulent boundary layer at the trailing edge of a NACA-0012 airfoil. The objective of the work is to provide a systematic analysis of the parameters, such as the number of exposures and enhancement steps, affecting the performance of MTE when investigating turbulent shear flows.

In the present work, it is chosen to evaluate the performance of the MTE technique directly on experiments, where the parameters governing the measurement accuracy are varied following the numerical simulations of Novara et al. (2010). Nevertheless, when dealing with experimental data, the exact distributions of the scattered light intensity and of the velocity field are unknown; therefore, the analysis of experimental errors becomes less straightforward in comparison with the computer simulated problem. The investigation is conducted making use of reference values obtained from optimal measurement conditions, when available (e.g., using a larger number of cameras). Otherwise, the performances of the MTE technique are evaluated from PIV relevant properties such as correlation signal-to-noise ratio (*S/N*), or from physical criteria applied to the specific flow conditions (expected shape of the space–time correlation function).

2 Working principle of the MTE technique

The motion tracking enhancement technique is based on the use of two or more tomographic recordings (sets of projections) in order to enhance the accuracy of the reconstruction of each recording. For double-frame recordings, the exposures are obtained at time instants t_1 and t_2. Between the two snapshots, particle images are displaced according to the flow motion in physical space projected onto the imagers. The basic idea of MTE is to consider the two recordings as separate projections of the same ensemble of particles, however, slightly distorted due to their motion with the flow. As a consequence, the approach may be able to virtually increase the number of views of the object.

Figure 1 illustrates the operating principle of MTE. Consider two particles A and B exposed at time t_1 and t_2. Their projections onto camera 1 and 2 are given in red and blue for the first and second exposure, respectively. Ghost particles (G_1, G_2) are formed at the intersection of the lines-of-sight corresponding to the particles. During the time interval between exposures, the relative position between particles and ghosts generally changes. As a result, deforming the particle field at time t_2 back into that at time t_1 (an estimator of the particle motion must be available) will make the actual particles superimpose, whereas the ghosts will not (Fig. 1-right). If the reconstructed particle field at time t_1 (E_1) is then combined with that at t_2 (E_2) mapped at time t_1 (pseudo-simultaneous object PSO_1), a first improvement is obtained, in fact, the ratio between ghosts and actual particles peak intensity is halved.

A second and more important improvement is obtained when the resulting intensity field is used as first guess in the MART algorithm to reconstruct the first exposure. The ghost particles from PSO_1 (G_2^*) that project onto image locations where the intensity is low (blue dots on the imagers, Fig. 1-right) will be rapidly discarded. Inverting
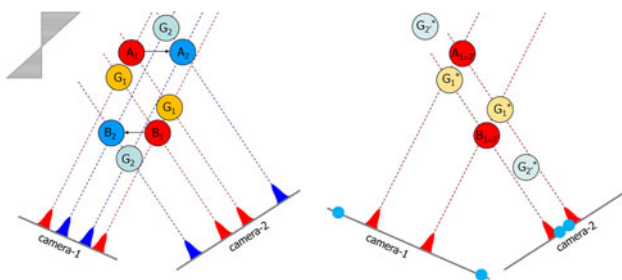
the order of the arguments, the same procedure can be used to improve the reconstruction of the second exposure.

Knowledge of the particle motion field is needed a priori to deform the reconstructed objects; therefore, the method requires a recursive implementation. In case of time-resolved PIV sequences, the procedure can also involve multiple exposures. Indicating with N_O, the number of considered exposures, with E_C the coherent (actual) intensity and with E_I the incoherent one (ghosts), an estimate was obtained by Novara et al. (2010) of the reduction in the ghost intensity within the enhanced guess E_G:

$$E_G \approx E_C + \frac{1}{N_O}\left(\sum_{n=1}^{N_o} E_{In}\right). \tag{1}$$

The iterative MTE algorithm can be summarized in a few steps:

1. MART reconstruction of individual recordings;
2. cross-correlation of reconstructed fields to obtain an estimate of the particles motion;
3. evaluation of the pseudo-simultaneous-objects by deforming the reconstructed fields;
4. linear combination of the objects with the relative PSOs to form the enhanced guess E_G;
5. MART reconstruction with object initialized with E_G.

The procedure is repeated until convergence of the results is observed; the number of MTE steps will be indicated in the following as N_E. A detailed description of the algorithm can be found in the work of Novara et al. (2010). The performance assessment, based on numerical simulation, proved the effectiveness of the method enabling seeding density three times higher than that currently used in Tomo-PIV experiments. The displacement fields obtained by 3D cross-correlation of the enhanced objects also showed a significant error reduction, with the situation further improving when more objects are employed (time series). Unless specified, results to numerical simulation mentioned in the following are referred to the study presented by Novara et al. (2010).

2.1 Computational cost of MTE

Considering that the data processing associated with the Tomo-PIV technique is already computationally intensive, the MTE method requires even higher computational resources. The combination of MTE with the acceleration techniques proposed by Atkinson and Soria (2009) resulted in an advanced method recently presented by Atkinson et al. (2010). In the present section, the essential computational aspects are discussed for the MTE technique. The tomographic reconstruction of two exposures and one three-dimensional cross-correlation between the intensity

Fig. 1 *Left*: reconstructed field at t_1 (*red*) and t_2 (*blue*), ghost particles in lighter colors. *Right*: enhanced guess for exposure 1 (displacement field in *gray*, superscript * indicates reduced intensity, *blue dots* in the image planes mark the position of back-projected intensity of ghosts from exposure 2 after deformation)

fields are needed to obtain a single velocity field. During reconstruction, the MART algorithm is repeated over 5 iterations. The 3D particle motion is evaluated by the volume deformation iterative multigrid technique (VO-DIM, Scarano and Poelma 2009) with typically three iterations of the cross-correlation analysis. Indicating with t_{MART}, the computation time needed for a single MART iteration, and with t_{CC}, the time needed for one cross-correlation iteration, the time required for the Tomo-PIV analysis of N_O exposures reads as follows:

$$t_{TOMO} = N_O \cdot t_{MART} \cdot N_{MART} + (N_O - 1) \cdot t_{CC} \cdot N_{CC} \qquad (2)$$

where N_{MART} indicates the number of MART iterations and N_{CC} the number of cross-correlation iterations. When the motion tracking technique is applied, the computational cost increases depending on the number of MTE iterations (N_E); in order to analyze the same number of exposures, if 10 enhancement steps are used, the total computational time needed is 10 times larger than the one needed by typical Tomo-PIV.

Nevertheless, since the reconstruction process is repeated for each MTE iteration, it has been observed that the MART iteration needed for each MTE step can be reduced from 5 to 2–3 iterations without affecting the reconstruction accuracy of the final enhanced objects. Furthermore, as shown in Sect. 3.1, 5 MTE iteration are sufficient to achieve the maximum improvement expected from MTE.

A possible reduction in the computational cost of cross-correlation analysis can be achieved if the multigrid procedure (interrogation box size refinement) is stopped at an earlier stage during the first MTE steps and extended to the full range only at the end.

It is estimated that the total computational time increases by approximately a factor 3 when the motion tracking enhancement technique is applied.

A further reduction in the computational time can be achieved making use of techniques such as the multiplicative first guess (MFG, Worth and Nickels 2008) or the multiple-line-of-sight (MLOS, Atkinson and Soria 2009) which have been shown to provide an acceleration of the reconstruction process over more than one order of magnitude.

At present, the computation time required for the analysis of a double-frame recording obtained with 4 megapixel cameras is in the order of 12 min for the MART analysis and 45 min when MTE is applied. The above figures are based on the use of LaVision DAVIS software, using a 8-core XEON PC with 2.66 GHz.

2.2 Effective volume for MTE

The efficiency of the MTE procedure in reducing the ghost intensity depends upon the particle motion field. It can be easily verified, for instance, that the ghost particles field produced by particles at rest cannot be reduced by the MTE approach, because the ghost particles move *coherently* with the actual particles. The same applies for particles traveling with exactly the same velocity. Only the incoherent intensity can be reduced in the process of evaluating the enhanced guess (Novara et al. 2010). A ghost pair occurs when the relative displacement between the particles producing the ghost varies by less than a particle image diameter d_τ in the direction normal to the viewing one. A model to estimate the number of recurring ghost particles (i.e., ghost pairs) in subsequent exposures, N_g^*, was formulated by Elsinga et al. (2010a, b); the ratio between N_g^* and the total number of *ghosts* is found to be proportional to l^*/l_z, where l_z is the reconstructed volume thickness and l^* is the fraction of depth along which the particles displacement varies less than d_τ.

We generalize here the approach for the purpose of defining a theoretical efficiency for the MTE technique. The volume V^* is the portion of the total volume V producing coherent ghost intensity. The complementary volume will be that effective for MTE, $V_{eff} = V - V^*$. The ratio V_{eff}/V provides an estimate of the MTE efficiency η_{MTE}. The numerical simulation produced by Novara et al. (2010) may be regarded as a case with $\eta_{MTE} \sim 1$ because the planar shear divides the measurement volume into slices of negligible thickness with respect to that of the overall volume. As a result, the application of MTE in the above conditions corresponds to a virtual multiplication of the number of viewing cameras N_C by the number of considered exposures N_O and yielding a system with $N_O \cdot N_C$ virtual views.

For experiments conducted at values of η_{MTE} below 1, the favorable effect of MTE is reduced. A theoretical estimate is given for the quality factor achievable with MTE that takes into account the effective volume. For a given number of exposures N_O, the reconstruction quality obtained with N_C cameras $Q_{MART}^{N_C}$ can be enhanced with MTE to $Q_{MTE}^{N_C}$ according to the expected efficiency as follows:

$$Q_{MTE}^{N_C} = Q_{MART}^{N_C} + \eta_{MTE} \cdot \left(Q_{MART}^{N_O \cdot N_C} - Q_{MART}^{N_C} \right). \qquad (3)$$

One may easily verify from Eq. 3 that when $\eta_{MTE} \to 1$ then $Q_{MTE}^{N_C} \to Q_{MART}^{N_O \cdot N_C}$, yielding the previously mentioned virtual camera multiplication effect. For the experimental conditions produced in the present study, when MTE is applied with 2 or more exposures, the value of $Q_{MART}^{N_O \cdot N_C}$ is very close to 1, which simplifies the evaluation of the relative reconstruction quality in the remainder. The above discussion is conducted under the simplifying hypothesis that the efficiency is a constant parameter only depending

upon the flow field. In principle, the efficiency will also depend upon the number of exposures N_O, whereby the integral effect of the particles motion causes the *ghost pairs* to loose coherence, which should further increase the value of the efficiency.

3 Experimental procedure and results

Two time-resolved experiments are conducted on turbulent shear flows in water and air flows. The PIV apparatus is based on a Quantronix *Darwin-Duo* Nd:YLF laser (2×25 mJ/pulse at 1 kHz) and four Photron *Fastcam* SA1 CMOS cameras ($1,024 \times 1,024$ pixels, 5,400 fps) equipped with Nikon objectives ($f = 105$ mm). Details on the jet experiments are reported by Violato and Scarano (2011), whereas the trailing edge boundary layer experiment is described in Ghaemi and Scarano (2011). In both cases, the system is operated in single-frame continuous mode to record time-resolved series. The synchronization, acquisition, and tomographic data analysis is performed by La-Vision *DaVis* 7.2 software on a PC equipped with INTEL dual quad-core 2.66 GHz CPU and 3 GB RAM memory.

3.1 Time-resolved measurements of a transitional jet

The flow is seeded with 56 microns polyamide particles at a concentration of approximately 0.7 particles/mm³. The jet exit diameter is 10 mm and the exit velocity is 0.45 m/s. A cylindrical volume of 30 mm diameter is illuminated from above the jet exit (Fig. 2-left). The cameras objectives are set at $f_\# = 32$ to obtain focused particle images along the entire depth of the illuminated volume. An optical magnification $M = 0.4$ yields a field of view of approximately 50×50 mm² and a digital resolution of 20 pixels/mm. The measurement domain extends from the jet exit up to 5 diameters downstream. The system records

sequences at 1,000 Hz. The raw images are processed subtracting the background intensity (estimated with local minimum over a spatial kernel of 31×31 pixels) and then the peak intensity is normalized taking the local maximum over 5×5 pixels regions. As a result, a background-free image is produced with rather uniform peak intensity for the particle images is obtained (Fig. 2-bottom-right).

The performance of the reconstruction algorithm, and therefore of the MTE technique, strongly depends on the image source density N_S. The latter can be obtained evaluating the number of particles per pixel (*ppp*) and estimating the area covered by each particle image. The number of imaged particles is systematically underestimated due to the finite probability of overlapping particles. From a numerical analysis based on synthetic generated images a density of 50,000 particles per Mpixel (particle imaged diameter of 3 pixels) causes a 10% underestimate of particles. In order to obtain a more accurate estimate of the seeding density, the illuminated region (Fig. 3-left) depth can be reduced by means of a knife-edge filter reducing the thickness of the illuminated volume in the Z direction from 30 to 5 mm (Fig. 3-right); the *ppp* is therefore reduced to 0.0077, where the estimate is considerably more accurate. The *ppp* (and in turn N_S) for full illumination is then computed detecting the particles in the low-density image and multiplying by the ratio of illuminated volumes. In the present case, the full volume is 6.5 times larger than that illuminated with the slit, which leads to an estimate of *ppp* = 0.05 for the full illumination case.

Given the particles image density (*ppp* = 0.05) and the particle imaged diameter $d_\tau^* = 3$ pixels, the resulting source density N_S is approximately 0.3.

Time-resolved measurement by four cameras shows that the velocity measured in potential flow regions yields a noise level below 0.03 voxels (0.5% V_{jet}). The jet flow undergoes first a Kelvin–Helmholtz like instability with the formation of vortex rings, which subsequently pair (*leap-*
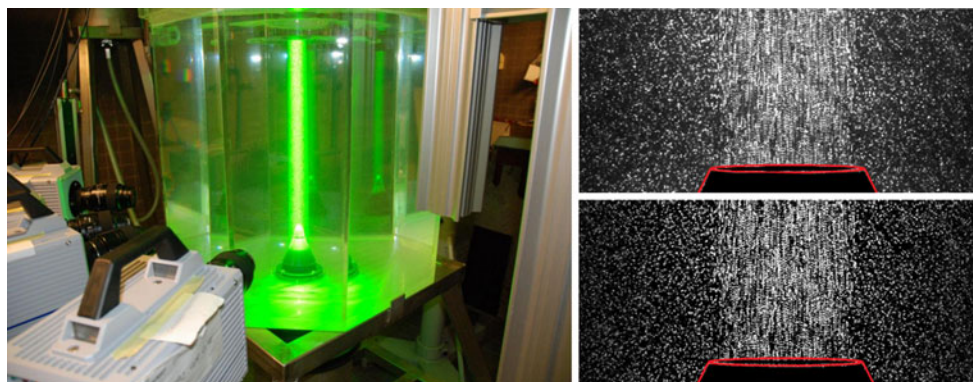

Fig. 2 *Left*: Jet tomography facility. *Right*: 5-exposure image of tomographic recordings above the jet exit (in *red*); (*top* raw image, *bottom* preprocessed)

Fig. 3 *Left*: detail of the illuminated region on the jet nozzle for circular illumination and recorded image on one camera ($ppp = 0.05$). *Right*: detail of the illuminated region on the jet nozzle for slit illumination and recorded image on one camera ($ppp = 0.0077$)
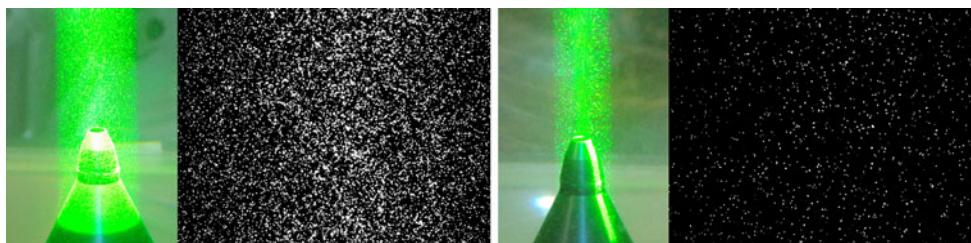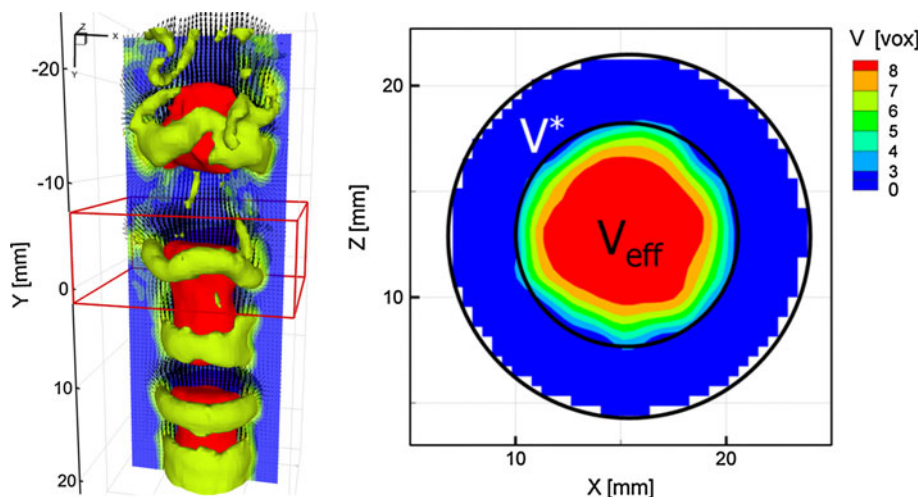

Fig. 4 *Left*: jet flow, instantaneous vorticity magnitude (0.2 1/s, *green*) and vertical velocity (0.35 m/s, *red*) iso-surfaces. Velocity vectors and vorticity magnitude contours on axial data slice. *Right*: iso-contours of axial velocity and indication of *ghost pairs*-producing volume V^* (*top view*)

frogging). Further away from the exit ($Y/D > 4$), the transition to the 3D regime is observed first with azimuthal wiggles in the vortex rings and then with the formation of vortex filaments inclined with respect to the jet axis. The red box in Fig. 4-left shows the region of flow considered for the present analysis; the reconstructed region extends over $501 \times 301 \times 392$ voxels. A large region of stagnant flow surrounds the jet core (Fig. 4-right); as a result, the ghost particles produced by the quiescent particles in the region $V^* = 0.6\,V$ will not be eliminated by MTE. The resulting MTE efficiency is estimated as $\eta_{MTE} = 0.4$.

3.1.1 Quality of tomographic reconstruction

For the present source density, given the absence of important optical aberrations, the good image contrast and the application of Volume Self-calibration (Wieneke 2008), the tomographic reconstruction by MART using 4 cameras provides an accurate estimate of the intensity fields, with an expected quality factor indicated by numerical simulations as beyond 0.9. If the number of cameras is reduced to three, numerical simulations indicate that the tomographic system should reach nearly the same performances of the 4-cameras system when MTE is applied.

Therefore, the result obtained with 4 cameras is taken as reference (E_{ref}) for comparison with that produced by the 3-cameras (E_{rec}) system with and without MTE. For such

purpose, a relative quality factor Q^* is introduced in this study as follows:

$$Q^* = \frac{\sum E_{ref} \cdot E_{rec}}{\sqrt{\sum E_{ref}^2 \cdot \sum E_{rec}^2}}. \tag{4}$$

Figure 5-left presents the evolution of the relative quality factor with the MART updates; double-frame and multi-frame modes have been considered here. Five MART iterations are used at the beginning of the reconstruction process; then, for each MTE step, a single MART update is applied. The improvement is more pronounced when more than 2 frames are considered. The result from $N_O = 3$ clearly departs from the two frames case and increasing the number of frames to 5 yields a marginal improvement, indicating that an asymptotic condition for N_O may have been reached. The results reach the value $Q^* \approx 0.83$, which indicates the maximum theoretical value to be expected on the basis of the estimated MTE efficiency (Eq. 3). A 5% uncertainty on the maximum expected value of Q^* has been included, taking into account the uncertainty in the estimate of the effective volume for MTE.

The improvement of the reconstruction quality can also be estimated without knowledge of a reference distribution, making use of the normalized intensity variance $\sigma_E^* = \sqrt{\overline{E'^2}}\big/\overline{E}$. The result is shown for MART and MTE-MART in Fig. 5-right; σ_E^* follows the same qualitative

Fig. 5 *Left:* relative quality factor with 3 cameras for MART and MTE-MART ($N_O = \{2,3,5\}$). Gray region indicating maximum Q^* expected by MTE for the given efficiency. *Right:* normalized intensity variance of the reconstructed field for MART and MTE-MART
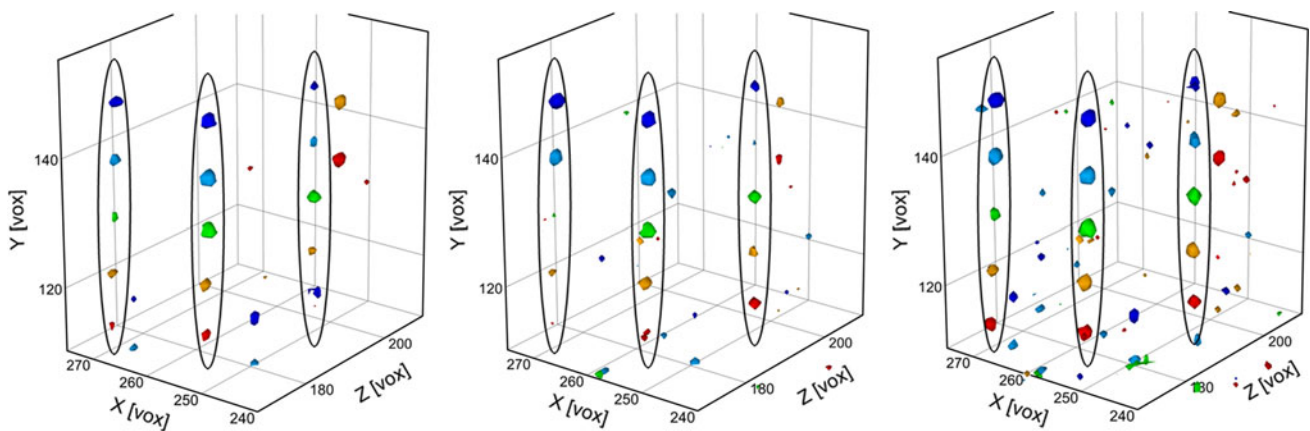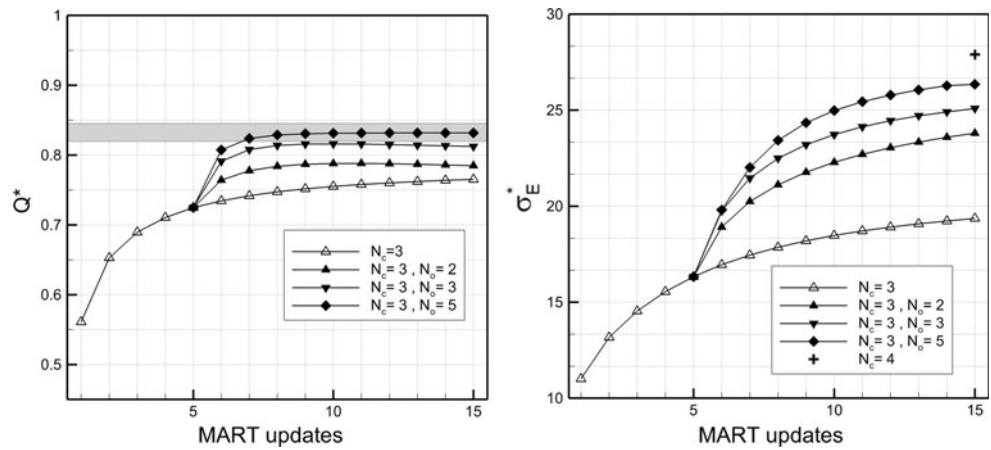

Fig. 6 Iso-surface of reconstructed intensity field (70 counts) in the center of the reconstructed region (jet core). Result from 5 MART updates with 4 cameras (*left*), 3 cameras (*middle*) and 3 cameras with 10 steps of MTE $N_O = 2$ (*right*). Particles color relative to time instant (t_1 *red*, t_5 *blue*, time separation of 1 ms)

behavior of Q^* along the updates, indicating the overall improvement of the reconstructed field. Higher values of σ_E^* indicate that the reconstructed particle intensity field will be more sparse and intensity peaks of higher amplitude emerge from the background intensity.

The numerical simulations showed that the main reason for the improved quality of reconstruction is the transfer of intensity from the ghosts to actual particles. This occurs because a ghost particle forms at the intersection of lines-of-sight which correspond to non-zero pixels. Therefore, the pixel intensity, which is the result of the projected actual particle intensity, is distributed among the actual and the ghost particle during the back-projection operation which is at the base of the MART algorithm. If the *ghost* intensity is diminished by MTE, the energy is redistributed toward the actual particle positions.

This behavior is qualitatively verified in the experiments observing the reconstructed field in time, which produces particle dots distributed along physical trajectories. A portion inside the jet core is considered, with particles

moving uniformly along straight lines and being detected at regular spatial intervals. Figure 6-left shows the intensity field reconstructed using MART and 4 cameras with 5 exposures color coded by time; several sequences are easily recognized (red to blue). Eliminating one camera, some particles disappear between subsequent exposures and then appear again. This behavior is ascribed to the more frequent occurrence (with respect to the 4-cameras system) of *ghost particles* which subtract intensity from those actual particles lying along the same line-of-sight. The reconstruction with the MTE technique exhibits a more regular distribution of the particle intensity along the sequence. This specific improvement suggests the possible use of MTE also to improve the reliability of particle motion analysis by PTV techniques (e.g., Schröder et al. 2009).

3.1.2 Cross-correlation analysis

Results from three-dimensional cross-correlation are presented in Fig. 7; velocity vectors and contours of axial

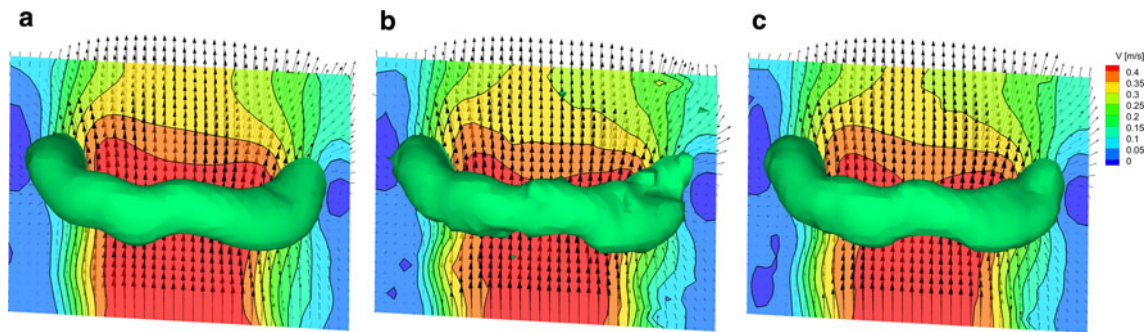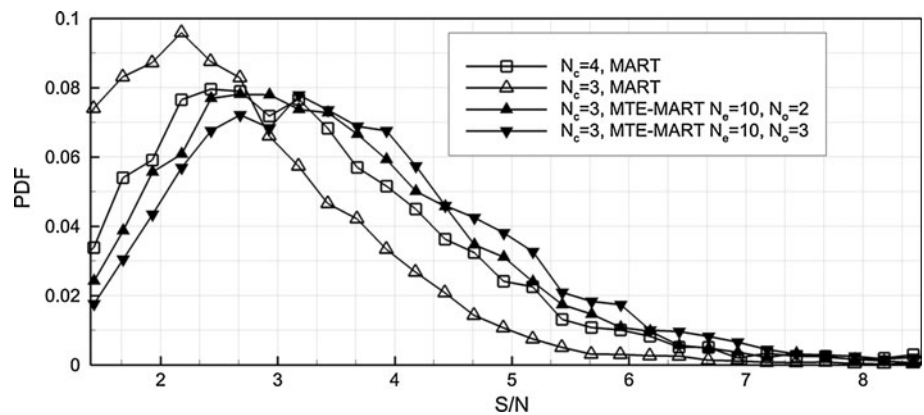**Fig. 7** Detail of the jet flow in proximity of a vortex ring. Iso-surface of Q, velocity vectors, and vertical velocity magnitude contours in data slice on the symmetry axis. **a** reference velocity field; **b** $N_C = 3$, $N_E = 0$; **c** $N_C = 3$, $N_E = 5$, $N_O = 3$

Fig. 8 Cross-correlation signal-to-noise probability density function for MART and MTE-MART

velocity are showed together with iso-surfaces of Q-criterion (Hunt et al. 1988). Cross-correlation analysis is performed by Volume Deformation Iterative Multigrid Technique (*VODIM*, Scarano and Poelma 2009) with a final interrogation volume of $40 \times 40 \times 40$ vox^3 with 75% overlap which gives a vector pitch of 0.5 mm. The same correlation settings have been used for each MTE iteration, including the first estimate of the velocity field. Vector validation based on the universal median test (Westerweel and Scarano 2005) is applied after each interrogation with an outlier detection rate of approximately 1.5%.

The reference velocity field is obtained by sliding multi-frame correlation (Scarano et al. 2010). The method makes use of four subsequent objects (three object-pairs) and produces averaged cross-correlation signals that significantly reduce random correlation errors. The flow time scale of the present experiment is approximately 30 ms and no amplitude modulation due to temporal filtering is expected with a kernel spanning 3 ms. When MART is applied with 3 cameras, the flow pattern closely resembles that obtained at $N_C = 4$. Nevertheless, the vortex visualized by the iso-surface of Q-criterion reveals a slightly higher noise level. The application of MTE appears less affected by irregularities indicating some degree of noise reduction.

A more marked difference is visible in term of correlation signal-to-noise ratio (Fig. 8). The introduction of MTE yields a generally higher value of correlation signal-to-noise ratio, indicating a more robust estimate of the reconstructed particles velocity. Moving from 4 cameras to three introduces a general drop of SN with the maximum shifting from 2.5 toward 2. A three cameras system appears to yield already SN of 2.5 with two objects, which is equivalent to four cameras. Using a triplet objects outperforms the four cameras system, with S/N above 3.

The velocity precision error is estimated by the root mean square of the relative difference to the reference data (multi-frame analysis); results are summarized in Table 1.

The error is reduced by about 15% when 5 steps of MTE are applied in double-frame mode; the reduction is slightly larger (approximately 20%) when 3 exposures are considered. Results are confirmed by the visual inspection of the time-history of the velocity components in a single point in the jet shear layer, where the discrepancy between the reference case and the 3 cameras case is reduced by the application of MTE (Fig. 9). It should be retained in mind that the error in this case is also due to finite number of particle in the interrogation volume and does not only depend upon the spurious reconstruction. Moreover, the low value of V^* limits the MTE efficiency for the jet flow

Table 1 Root mean square of the velocity error relative to the reference for MART with 3 and 4 cameras and MTE-MART ($N_E = 5$) with 3 cameras

	$(U - U_{ref})_{RMS}$ (voxels)	$(V - V_{ref})_{RMS}$ (voxels)	$(W - W_{ref})_{RMS}$ (voxels)
MART $N_c = 4$	0.17	0.2	0.18
MART $N_c = 3$	0.22	0.27	0.23
MTE-MART $N_c = 3$, $N_o = 2$	0.19	0.23	0.19
MTE-MART $N_c = 3$, $N_o = 3$	0.18	0.22	0.18

Fig. 9 Time-history of the velocity components along 100 exposures in one point in the jet shear layer
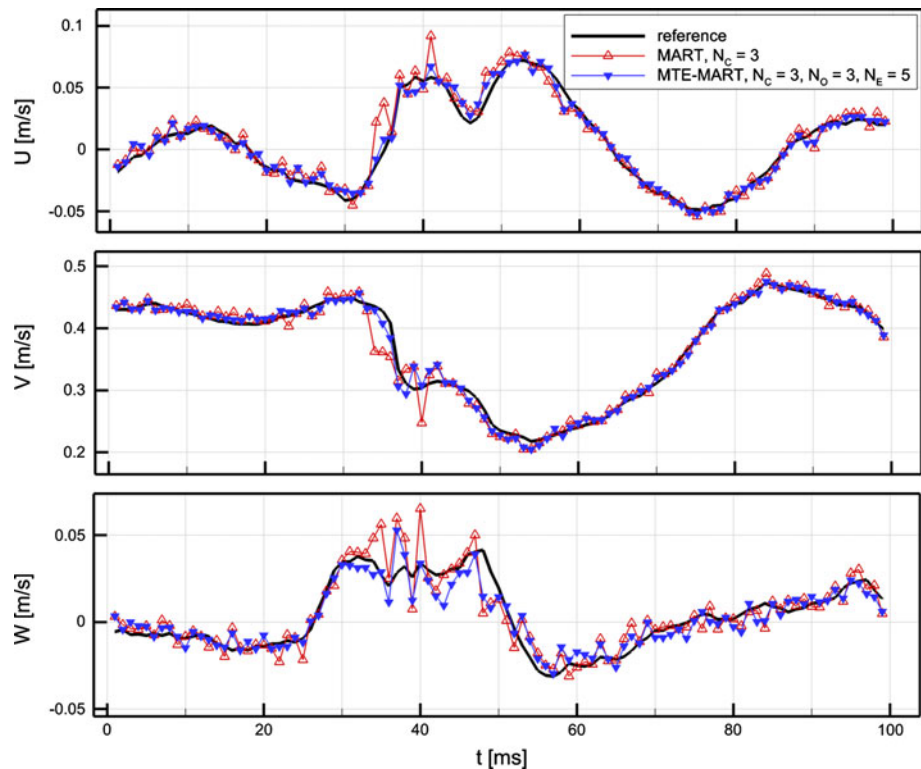
configuration. Therefore, the marginal improvements are expected. The reconstruction from the 3-camera system is already rather close to that with 4 cameras for the present seeding density. As a consequence, the velocity measurement error becomes dominated by the cross-correlation analysis rather than by artifacts introduced in the reconstruction. Nevertheless, it is proven that the trend is consistent with that of the numerical simulations and in this case MTE dose bring some measurable increase of measurement accuracy.

3.2 Turbulent boundary layer

The experiment is performed in a low-speed wind tunnel where a NACA-0012 airfoil of 40-cm chord is installed at zero angle of attack. The free-stream velocity is 14 m/s and the Re_c is 370,000. Light amplification is provided by the use of mirrors reflecting the beam multiple times forming an extended illuminated domain, Fig. 10-left (Ghaemi and

Scarano 2010). The depth of the illuminated volume is 8 mm. The imaging system is set with numerical aperture $f_\# = 22$. In the chosen reference system, Z indicates the direction normal to the airfoil surface ($Z = 0$ mm), X and Y are aligned with the streamwise and spanwise directions, respectively. The field of view is approximately 40×25 mm^2 in the streamwise and spanwise direction, respectively, and it is located at the trailing edge of the airfoil. The digital resolution is 20 pixels/mm, and the acquisition frequency is 12 kHz.

A fog generator produces droplets of 1 μm diameter; given the present imaging conditions, the observed particle image diameter d_τ is 2 pixels. Two experiments are conducted at different seeding density; the first one with approximately 3 particles/mm^3, corresponding to a ppp of 0.05 (example of recorded image in Fig. 10-middle-top), while the second is well beyond this value, Fig. 10-middle-bottom. Given the relatively small particle image diameter, the seeding density can be obtained by detection of imaged
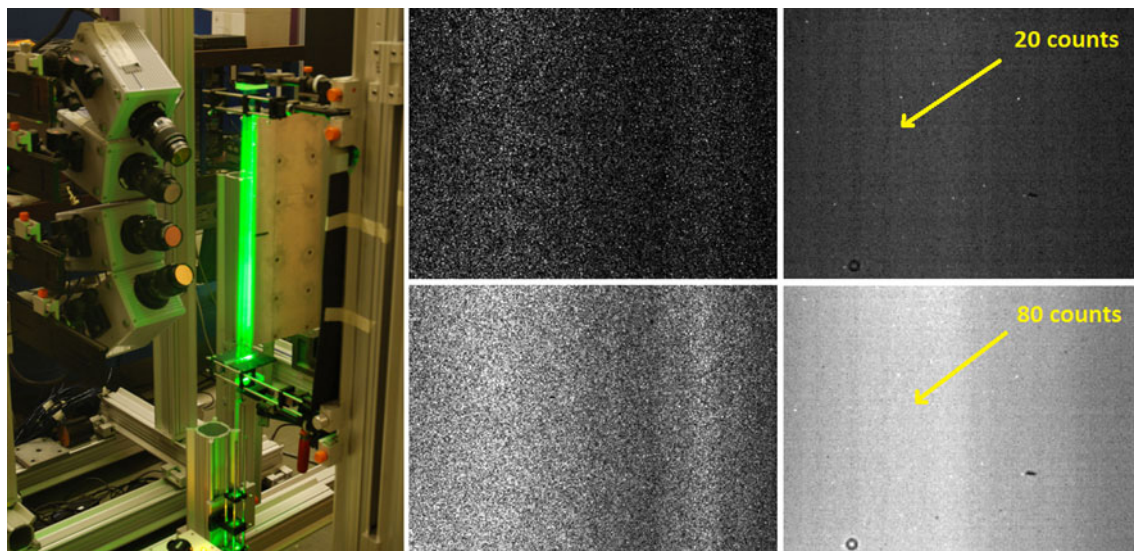
Fig. 10 *Left:* Tomographic PIV setup. *Top-middle*: detail of Tomo-PIV image for the boundary layer experiment at $ppp = 0.05$. *Bottom-middle*: image at $ppp = 0.2$. *Top-right* mean imaged intensity over 200 images at $ppp = 0.05$. *Bottom-right*: mean imaged intensity over 200 images at $ppp = 0.2$

particles for the first experiment. This is not the case for the latter due to overlapping particles. In order to estimate the seeding density, the average intensity over 200 images has been considered; the distribution of average intensity over the image is rather uniform and equal to approximately 20 counts for the low-density case (Fig. 10-top-right). The same operation leads to 80 counts for the high-density case meaning that the particle concentration in the second case is approximately 4 times higher than the first one, leading to a seeding density of approximately 12 particles/mm^3 ($ppp = 0.2$). The source density N_S is 0.15 and 0.6 for the low- and high-density case, respectively. The latter condition is recognized as beyond optimum for a tomographic system with 4 cameras (Novara et al. 2010).

Figure 10-middle shows pre-processed images at $ppp = 0.05$ and raw images at 0.2, where pre-processing is not performed because the background intensity cannot be separated from the signal produced by the actual particles.

The domain is discretized into $890 \times 550 \times 200$ voxels and reconstructed using 5 MART iterations for both the seeding densities; motion tracking enhancement is applied making use of 10 steps, and 2 MART iterations are used for each enhancement step. The effective volume V_{eff} is estimated to be above 90% of the total ($\eta_{MTE} > 0.9$); as shown in Fig. 11, the investigated domain is in fact completely within the turbulent boundary layer ($\delta_{99} = 9.5$ mm). The cross-correlation analysis applies multi-grid with final interrogation volume of $24 \times 24 \times 24$ voxels ($1.2 \times 1.2 \times 1.2$ mm^3). With 75% overlap factor, the vector pitch is 0.27 mm. For the given block size and particle concentration, the analysis counts on average 4 and 15 particles within the interrogation box for the low and high seeding,
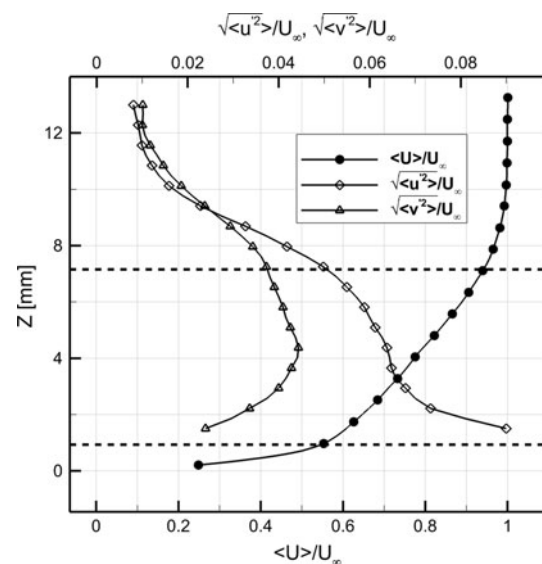

Fig. 11 Boundary layer mean streamwise velocity component and fluctuating velocity profiles data obtained from two-components PIV (Ghaemi and Scarano 2011); *dotted lines* indicate the measurement domain for the Tomo-PIV experiment

respectively. The same correlation settings and validation by universal median test (Westerweel and Scarano 2005) used for the final interrogation analysis have been used for the velocity field estimate at each intermediate MTE iterations.

The instantaneous velocity field (raw velocity vectors) is shown in Fig. 12-top on a data slice 2.6 mm above the airfoil surface. A uniform velocity (80% of the free-stream) is subtracted to highlight the pattern of local fluctuations. Contours of the wall-normal component of vorticity are displayed in the background. The flow pattern returned by
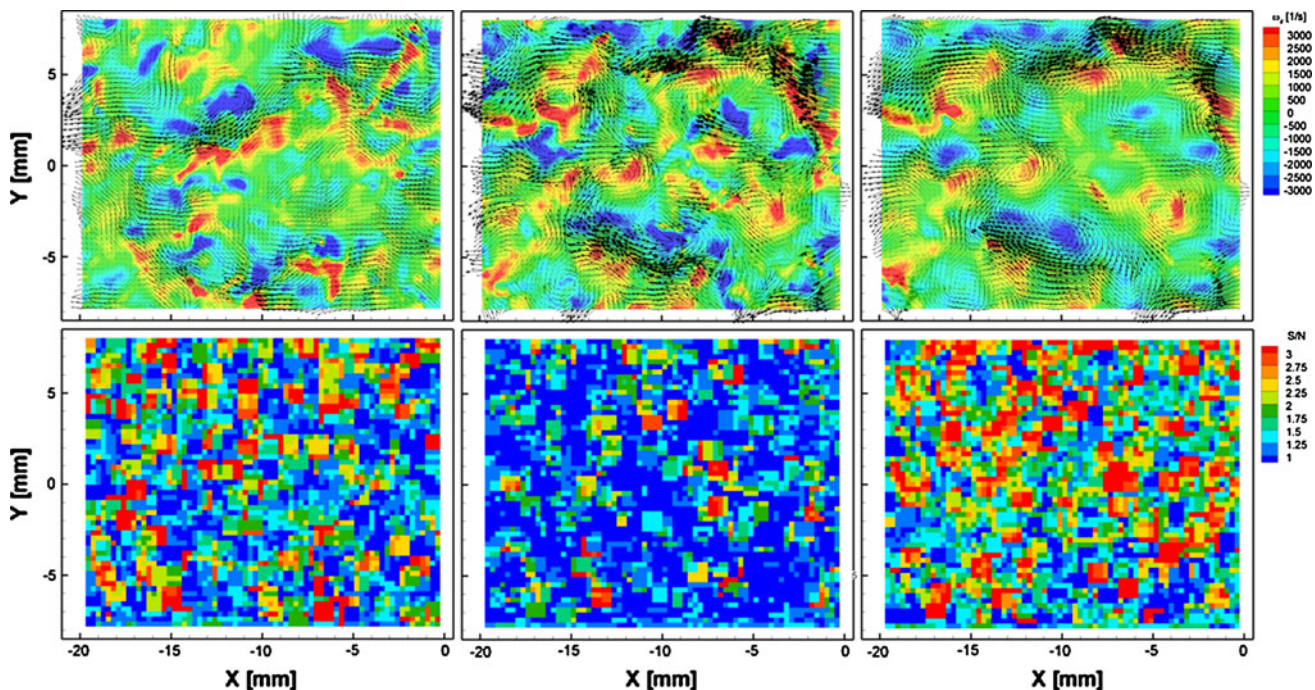
Fig. 12 Detail of turbulent boundary layer at $Z = 2.6$ mm. *Top* relative velocity vectors and *z*-vorticity contours. *Bottom S/N. Left ppp* = 0.05, MART. *Middle ppp* = 0.2, MART. *Right ppp* = 0.2, MTE-MART, $N_E = 10$, $N_O = 2$

the low-density experiment reveals alternating low- and high-speed regions; counter-rotating swirling patterns identified in the velocity vector field suggest the presence of hairpin vortexes (Fig. 12-top left).

The number of particle tracers present in each interrogation volume appears to be sometimes insufficient for the given seeding concentration, which is revealed by a blocky pattern with rather constant velocity due to the combined effect of signal loss and the overlap factor between neighboring volumes (oversampling). The distribution of cross-correlation signal-to-noise ratio below 1.5 by more than 50% of the measurement domain confirms indirectly the above observation (Fig. 12-bottom left).

When the experiment is performed at higher seeding density, the results based on MART reconstruction (Fig. 12-middle) yield a similar flow arrangement but a higher level of spurious fluctuations is evident from the vorticity peaks and from groups of vectors clearly out-of-pattern. The signal-to-noise drops further and is close to 1 nearly everywhere, indicating that the correlation signal is largely affected by reconstruction noise. These conditions would typically be avoided for a Tomo-PIV experiment designed upon the MART reconstruction technique.

The motion tracking enhancement is applied to the same recordings making use of 2 exposures by 10 steps resulting in the velocity field and correlation S/N are shown in Fig. 12-right. A significant increase in the correlation signal (typically a factor 2 with respect to the MART analysis)

indicates that ghosts are largely reduced ($S/N > 1.5$ in more than 60% of the measurement volume) resulting in a more robust estimate of the particles motion. Also the measurement accuracy appears increased, with a more coherent velocity and vorticity fields.

A quantitative assessment of the measurement precision is made invoking the physical principle that velocity fluctuations are convected by the flow and their typical evolution time is significantly longer than the measurement inter-framing time ($\Delta T = 83.3$ μs). Assuming Taylor's hypothesis of *frozen turbulence* to be valid within such inter-framing time, we can obtain an estimate of the measurement precision error from the analysis of the spatio-temporal correlation function peak height. Cenedese et al. (1991) investigated the validity of this assumption in a highly turbulent flow with the general conclusion that the hypothesis holds valid for large flow structures and small time separation. Following Tennekes (1975), the Lagrangian de-correlation time scale of turbulent fluctuations for isotropic turbulence is estimated around 10 ms for the present case, which is two orders of magnitude longer than ΔT. As a consequence, no significant loss of correlation is expected between subsequent velocity fields along a time series for more than 10 exposures.

The space–time correlation function ϕ is evaluated for each of the velocity components. After mean subtraction, the correlation of the velocity *x*-component between two subsequent exposures separated by a time delay τ reads as:

$$\phi_u(\mathrm{d}x, \mathrm{d}y, \mathrm{d}z, \tau)$$

$$= \frac{\sum_{i,j,k=1}^{M} u(i,j,k,t) \cdot u(i+\mathrm{d}x, j+\mathrm{d}y, k+\mathrm{d}z, t+\tau)}{\sqrt{\sum_{i,j,k=1}^{M} (u(i,j,k,t))^2 \cdot \sum_{i,j,k=1}^{M} (u(i,j,k,t+\tau))^2}} \quad (5)$$

where M is the kernel of the considered interrogation volume and τ indicates the time separation, and the displacements $\mathrm{d}x$, $\mathrm{d}y$, and $\mathrm{d}z$ are expressed in measurement grid units. The displacement of the turbulent structures between two subsequent realizations is also accounted for applying a relative shift between interrogation boxes in the streamwise direction based on the estimated convective velocity (11.2 m/s). The height of the correlation peak, indicated by $\phi_{\max}$, is obtained as the maximum of the correlation function. Under these hypotheses the height of the correlation peak is expected to maintain unit value, except for the uncorrelated component of the signal, which is then ascribed to the measurement precision error $\bar{\varepsilon} \propto (1 - \overline{\phi}_{\max})$, where $\overline{\phi}_{\max}$ is the mean value of the correlation map peak (Table 2).

The mean value of the correlation peak height $\overline{\phi}_{\max}$ has been evaluated for several values of the time delay between measurements τ (Eq. 5), also to verify the validity of frozen turbulence (Fig. 13). After dropping from unit value (by definition in the origin) to the value of the first sample at $\tau = 83.3\ \mu s$, the correlation height remains practically constant up to separations beyond 1 ms. This confirms that the loss of coherence is dominated by uncorrelated noise affecting the velocity field measurement rather than by the evolution of the flow.

Therefore, the difference between results obtained at low- and high-seeding density is only ascribed to measurement precision errors. The probability density function (PDF) of the correlation peak height reveals that the measurements performed at low-seeding density are
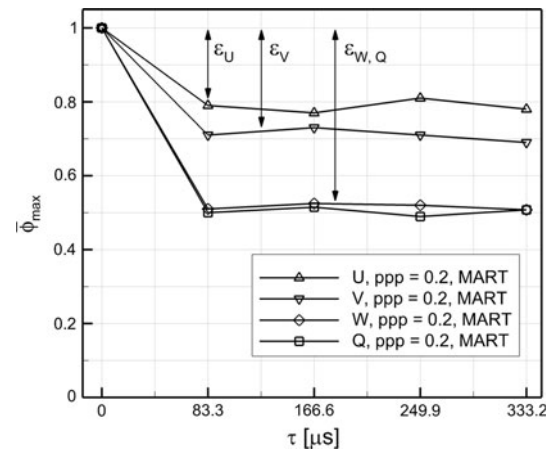

Fig. 13 Mean correlation peak height ($\overline{\phi}_{\max}$) and mean precision error ($\bar{\varepsilon}$) increasing time delay between exposures for the velocity components and the Q-criterion

weaker than that at high-density when analyzed with MTE-MART (Fig. 14). By coincidence, the PDF of the low-density case appears to be similar to that at $ppp = 0.2$ when only MART is applied, which is ascribed to a combination of effects. In the low-seeding case, too few particles are included in the interrogation boxes, and the error is dominated by the cross-correlation noise. In the high-seeding case, the information density is higher; but the ghost component affects the result more widely. The streamwise velocity component fluctuations exhibit the highest correlation (Fig. 14-left). In contrast, the spanwise component shows a less pronounced peak at 0.95 for the MTE analysis and below 0.9 and 0.8 or the MART analysis of the high- and low-seeded case, respectively. The most critical component is w, showing a flat distribution, because of the combined effect of its relatively small range of fluctuations (approximately 2 voxels) and the larger

Table 2 Spatial mean of the cross-correlation function peak value ($\overline{\phi}_{\max}$) for MART and MTE-MART ($N_E = 10$, $N_O = 2$) at $ppp = 0.05$ and 0.2 for velocity components, vorticity components and Q-criterion

	$ppp = 0.2$		$ppp = 0.05$		
	MART $v_S = 24^3$ vox	MTE-MART $v_S = 24^3$ vox	MART $v_S = 24^3$ vox	MTE-MART $v_S = 24^3$ vox	MART $v_S = 32^3$ vox
$\overline{\phi}_{\max, u}$	0.79	0.87	0.74	0.76	0.85
$\overline{\phi}_{\max, v}$	0.71	0.76	0.66	0.67	0.77
$\overline{\phi}_{\max, w}$	0.51	0.62	0.55	0.55	0.62
$\overline{\phi}_{\max, \omega_x}$	0.53	0.61	0.55	0.56	0.67
$\overline{\phi}_{\max, \omega_y}$	0.53	0.61	0.5	0.5	0.64
$\overline{\phi}_{\max, \omega_z}$	0.72	0.78	0.7	0.72	0.84
$\overline{\phi}_{\max, Q}$	0.5	0.57	0.47	0.48	0.6

Interrogation volume size used for the cross-correlation of reconstructed object indicated with v_S
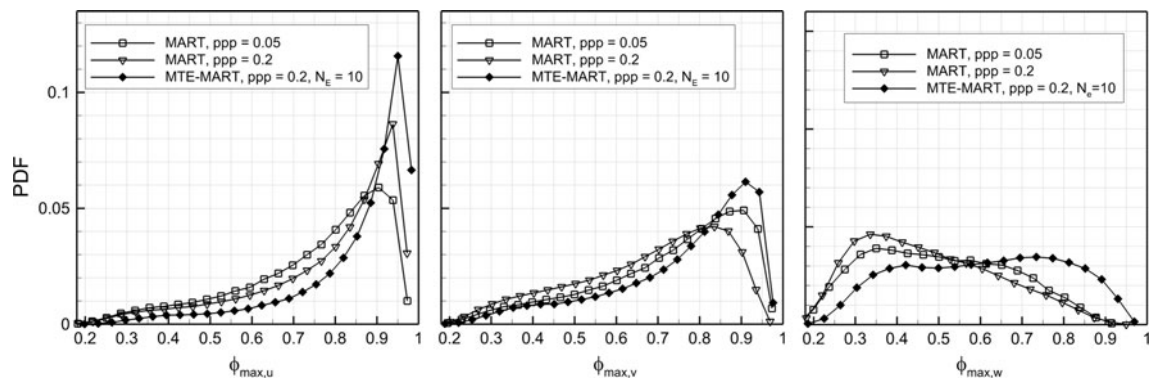
Fig. 14 Probability density function of the peak value of the space–time correlation map between two subsequent velocity fields

absolute uncertainty resulting from the geometry of the tomographic system.

In conclusion, the MTE analysis of the high-seeding case appears to offer a significant increase in the space–time correlation peak height. The estimated reduction in the precision error is approximately 40% for the streamwise component and somewhat less for v and w. Instead, at $ppp = 0.05$, only a marginal improvement is obtained, which is consistent with the above discussion. To make a fair comparison between the low- and high-seeding density cases, the interrogation volume is increased by more than a factor two (interrogation box of 32^3 voxels), which brings the average number of particles per interrogation box up to 9. This condition guarantees a more robust correlation analysis at the cost of a lowered spatial resolution. In this case, the analysis performed with MART yields results an estimate of the precision error that approaches that of MTE-MART obtained with an interrogation of 24^3 voxels.

Time-resolved Tomo-PIV is often used to visualize the temporal evolution of turbulent structures in the boundary layer (Schröder et al. 2008; Elsinga et al. 2008). In the present case, a low-speed region and a single hairpin vortex are selected and tracked in time. A qualitative inspection of the time series at high-seeding density is shown in Fig. 15. The evolution of a low-speed streak, detected by means of iso-surface of streamwise velocity ($U = 10$ m/s), along 4 subsequent exposures is presented together with iso-surfaces of W component that indicate the ejection events distributed above the streak. As indicated by the spatio-temporal correlation analysis, the result obtained by MTE (Fig. 15-right) shows a reduction in measurement noise and an increased temporal coherence. The same applies for the vortical structures (Fig. 16); a detail of the boundary layer is extracted where a hairpin vortex is convected during four snapshots (total observation time 3.3 ms). The result is presented as a sequence of snapshots color coded in time (red to blue) for clarity. As detection criterion, the Q-criterion iso-surface is chosen. The result obtained with the MART reconstruction shows the hairpin structure,

however, embedded in a dense noisy pattern hiding several details of the vortex topology. The MTE-MART analysis removes the noisy fluctuations to a large extent and details such as hairpin legs with two different inclination angles become more clear, resulting also in an overall higher temporal coherence. The latter effect is not ascribed to a different spatial resolution of the MTE-MART since the same size of interrogation box is used for the comparison. Nevertheless, further judgments in this regard could be made examining the energy spectrum of if the turbulent energy fluctuations in the frequency domain, which is not available with the current experiment.

4 Conclusions

The motion tracking enhancement technique was applied to Tomographic PIV experiments in turbulent shear flows. For the transitional jet in water the analysis with a 3-cameras system is compared with reference results obtained with an additional camera. The application of MTE increases the relative quality of reconstruction as a function of the number of exposures used in the enhancement process. The concept of MTE efficiency has been also introduced along with a model to predict the reconstruction performance increase from MTE. The experimental verification yields an increase nearly reaching the theoretical prediction and the precision error is decreased of about 20%.

In the air flow experiment of turbulent boundary layer, a seeding density of approximately 4 times higher than currently practiced ($ppp = 0.2$) is obtained. Results show that MTE largely improves the robustness of the measurement increasing the cross-correlation signal-to-noise from below 1.5 to 3. The height of the spatio-temporal correlation function between subsequent time instants has been taken as an indicator of the accuracy of the measurement. Significant improvements are observed in this case, with 40% reduction in the precision error for the streamwise velocity
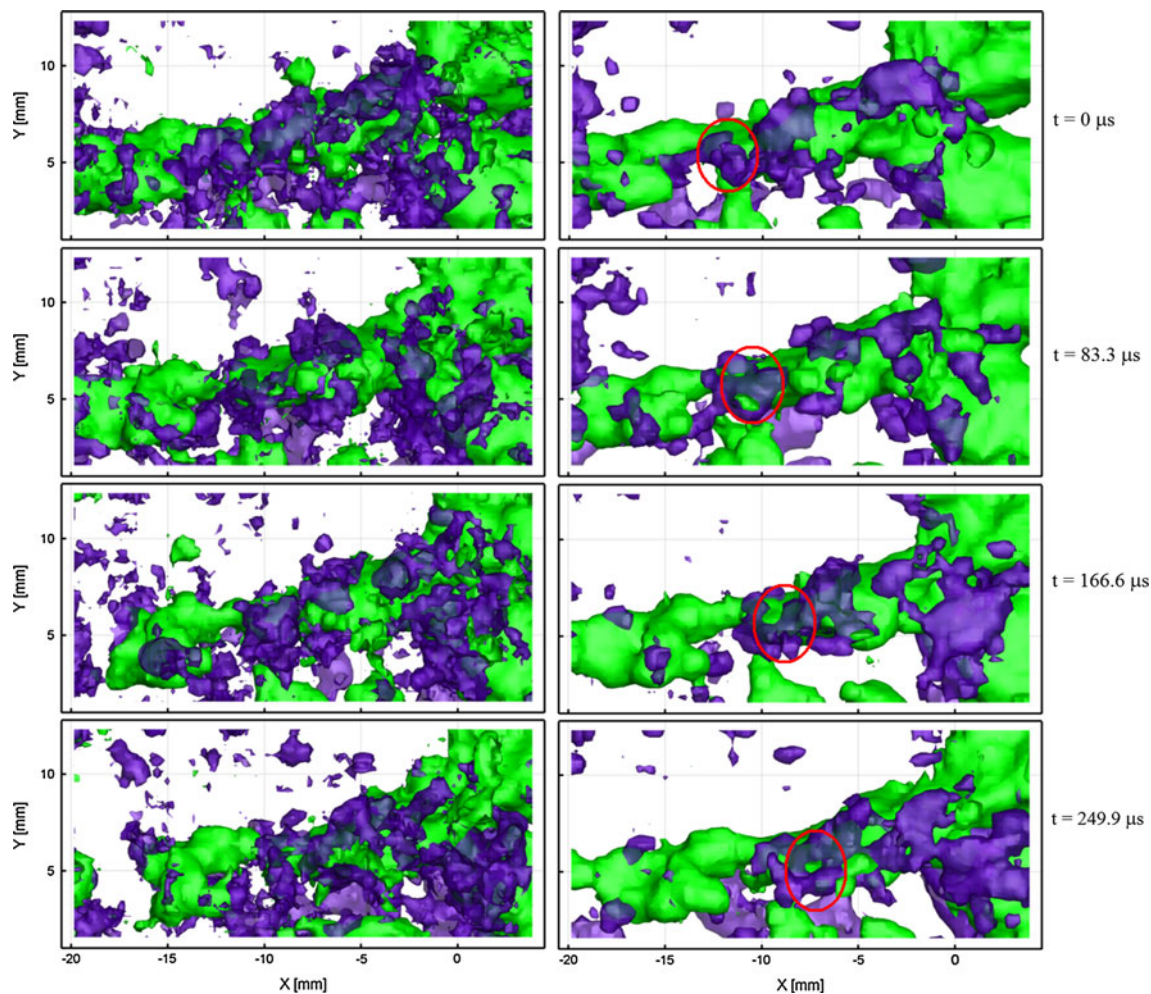
Fig. 15 Evolution of a low-speed streak along 4 subsequent time instants for MART (*left*) and MTE-MART (*right*). Iso-surface of streamwise velocity ($U = 10$ m/s) in *green* and of wall-normal component ($W = 1$ m/s) in *blue*. *Red circle* indicates the same ejection event in the 4 realizations
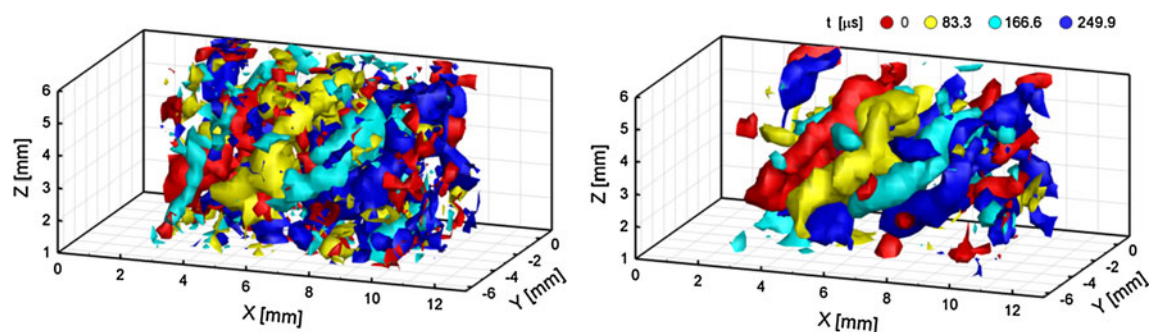

Fig. 16 A hairpin vortex convected along four exposures (*red, yellow, light blue,* and *blue*). Iso-Q surfaces for MART (*left*) and MTE-MART (*right*). Iso-surface of streamwise velocity ($U = 10$ m/s) in *green*

component and approximately 20% for the other components. Also for derived quantities such as vorticity and vortex detection based on the Q-criterion, the MTE technique yields more clear description of the topology of coherent structures and their temporal evolution.

References

Adrian RJ (1991) Particle-imaging techniques for experimental fluid mechanics. Ann Rev Fluid Mech 23:261–304

Atkinson C, Soria J (2009) An efficient simultaneous reconstruction technique for tomographic particle image velocimetry. Exp Fluids 47:553–568

Atkinson C, Buchmann MS, Soria J (2010) Adaptive MLOS-SMART improved accuracy tomographic PIV. In: Proceedings of 15th international symposium on applications of laser techniques to fluid mechanics, Lisbon, Portugal, 7–10 July

Cenedese A, Romano GP, Di Felice F (1991) Experimental testing of Taylor's hypothesis by L.D.A. in highly turbulent flow. Exp Fluids 9:351–358

Coëtmellec S, Buraga-Lefebvre C, Lebrun D, Özkul C (2001) Application of in-line digital holography to multiple plane velocimetry. Meas Sci Technol 12:1392–1397

Elsinga GE, Scarano F, Wieneke B, van Oudheusden B (2006) Tomographic particle image velocimetry. Exp Fluids 41:933–947

Elsinga GE, Wieneke B, Scarano F, Schröder A (2008) Tomographic 3D-PIV and applications, in particle image velocimetry—new developments and recent applications. In: Schröder A, Willert C (eds) Topics in applied physics, vol 112. Springer, Berlin

Elsinga GE, Adrian RJ, van Oudheusden BW, Scarano F (2010a) Three-dimensional vortex organization in a high-Reynolds-number supersonic turbulent boundary layer. J Fluids Mech 644:35–60

Elsinga GE, Westerweel J, Scarano F, Novara M (2010b) On the velocity of ghost particles and the bias error in Tomographic PIV. Exp Fluids 50:825–838

Ghaemi S, Scarano F (2010) Multi-pass light amplification for tomographic particle image velocimetry applications. Meas Sci Technol 21:127002

Ghaemi S, Scarano F (2011) Counter-hairpin vortices in the turbulent wake of a sharp trailing edge. J Fluid Mech (under review)

Herman GT, Lent A (1976) Iterative reconstruction algorithms. Comput Biol Med 6:273–294

Humble RA, Elsinga GE, Scarano F, van Oudheusden BW (2009) Three-dimensional instantaneous structure of a shock wave/boundary layer interaction. J Fluids Mech 622:33–62

Hunt JCR, Wray AA, Moin P (1988) Eddies, stream, and convergence zones in turbulent flows. Technical report, Center for Turbulence Research

Maas HG, Gruen A, Papantoniou D (1993) Particle tracking velocimetry in three-dimensional flows. Exp Fluids 15:133–146

Novara M, Batenburg KJ, Scarano F (2010) Motion tracking enhanced MART for tomographic PIV. Meas Sci Technol 21:035401

Pereira F, Gharib M (2002) Defocusing digital particle image velocimetry and the three-dimensional characterization of two-phase flows. Meas Sci Technol 13(2002):683–694

Petra S, Schröder A and Schnörr C (2009) 3D tomography from few projections in experimental fluid dynamics. Imaging Meas Methods (NNFM), vol 106, Springer, Berlin, pp 63–72

Scarano F, Poelma C (2009) Three-dimensional vorticity patterns of cylinder wakes. Exp Fluids 47:69–83

Scarano F, Elsinga GE, Bocci E, Van Oudheusden BW (2006) Investigation of 3-D coherent structures in the turbulent cylinder wake using Tomo-PIV. In: Proceedings of 13th international symposium on applications of laser techniques to fluid mechanics, Lisbon, Portugal, 26–29 June

Scarano F, Bryon K, Violato D (2010) Time-resolved analysis of circular chevron jets transition by Tomo-PIV. In: Proceedings of 15th international symposium on applications of laser techniques to fluid mechanics, Lisbon, Portugal, 7–10 July

Schröder A, Geisler R, Elsinga GE, Scarano F, Dierksheide U (2008) Investigation of a turbulent spot and a tripped turbulent boundary layer flow using time-resolved tomographic PIV. Exp Fluids 44:305–316

Schröder A, Geisler R, Sieverling A, Wieneke B, Henning A, Scarano F, Elsinga GE, Poelma C (2009) Lagrangian aspects of coherent structures in a turbulent boundary layer flow using TR-Tomo PIV and PTV. In: Proceedings of 8th international symposium on particle image velocimetry, Melbourne, Victoria, Australia, 25–28 Aug

Tennekes H (1975) Eulerian and Lagrangian time microscales in isotropic turbulence. J Fluid Mech 67(Part 3):561–567

Violato D, Scarano F (2011) Three-dimensional evolution of flow structures in transitional circular and chevron jets. Phys Fluids (to appear)

Westerweel J, Scarano F (2005) Universal outlier detection for PIV data. Exp Fluids 39:1096–1100

Wieneke B (2008) Volume self-calibration for 3D particle image velocimetry. Exp Fluids 45:549–556

Worth NA, Nickels TB (2008) Acceleration of Tomo-PIV by estimating the initial volume intensity distribution. Exp Fluids 45(5):847–856